

# A Study of Coronary Artery Disease in the Left Circumflex Artery via Artificial Vessel Restoration

Akhil Paulraj <sup>1</sup>, Fei Liu <sup>2</sup>

<sup>1</sup> *West Windsor-Plainsboro High School North, akhilcpaulraj@gmail.com*

<sup>2</sup> *New Jersey Science Academy*

May 27, 2020

## Abstract

In recent years, computational fluid dynamics techniques have been employed to advance the understanding of cardiovascular flows and have been largely focused on wall shear stress (WSS) and the effect of disturbed flows on atherosclerosis, and in turn, coronary artery disease (CAD). To gain further insight into the hemodynamics associated with CAD, numerical simulations were conducted on a diseased left circumflex artery (LCX). The vessel geometry was derived from computed tomography angiography (CTA) data of a diseased LCX vessel. The diseased vessel was then artificially restored to represent its initially healthy geometry, and simulations were re-run for comparison. It was determined that alongside the expected low WSS, a region of high vorticity was present at the location where CAD developed, resulting in disturbed blood flow. The vorticity may also be associated with the curvature of the vessel. The relevance of the observed characteristics was further supported by perturbing the geometry of the restored LCX via dilation to account for inaccuracies in the restoration process. This research suggests that vorticity is an important factor in assessing the risk for CAD, potentially improving the accuracy of non-invasive, computational diagnosis. In turn, as computational analysis of the coronary arteries improves, it is likely that unnecessary invasive diagnosis methods, such as an angiogram, can be avoided.

## 1 Introduction

Cardiovascular disease is the leading cause of death in the United States, reported by Benjamin et al. [2019] from the American Heart Association. CAD is the most common type of heart disease, and 6.7% of all adults in the United States over the age of 20 have CAD [Benjamin et al., 2019]. To garner more knowledge about cardiovascular disease and specifically CAD, computational methods have been employed as a research tool to study the fluid dynamics of cardiovascular flows.

Research on cardiovascular flows began with Leonardo da Vinci in the 15th century, who worked on in vivo studies with pigs to examine the flow of blood. da Vinci also constructed physical glass models of the heart and drew comparisons with the dynamics of water; in this manner, he recognized the importance of hemodynamics when studying cardiovascular flow [Sterpetti, 2019]. The basis of modern views of the cardiovascular system is rooted in the work of William Harvey, who was the first to both recognize and document his discovery of blood circulation [Parker, 2009]. Research on atherosclerosis, and in turn CAD, truly began only in the 19th century, as researchers began to hypothesize about the importance of WSS and flow separation. For many years, there existed a controversy between two contradicting hypotheses. One explanation argued that high WSS favors atherogenesis due to the mechanical damage caused by high WSS in the endothelium. The other explanation argued that low WSS favors atherogenesis because it is associated with arterial wall mass transport [Dhawan et al., 2010]. It has since been established that the second hypothesis is correct, also implying the significance of low WSS in the development of CAD [see Heo et al., 2014, Chiu and Chien, 2011, Nigro et al., 2011]. Disturbed blood flow in arterial bifurcations, branch ostia, and curvatures have also been shown to be prone to atherosclerosis [Nigro et al., 2011].

A more complete understanding of the hemodynamics contributing to the development of CAD is needed to improve upon existing risk analysis and diagnosis methods. By improving the accuracy of simulation-based methods, patients will have access to a cheaper, and often more accurate, way to be diagnosed.

The standard method for the diagnosis of patients with CAD is invasive coronary angiography (ICA) [Hulten and Carlson, 2013]. In ICA, a catheter is inserted into an artery, a dye is injected through the catheter into the coronary arteries, and X-Ray images are taken to inspect the vessels in question. Despite being the current standard for diagnosis, ICA has many drawbacks; for example, there may be complications that result from the invasive nature of ICA including site bleeding, deterioration of renal function, (cerebral) embolism and allergic reactions [Borren et al., 2015]. In addition, ICA is often unnecessary altogether: multiple registries have recognized that ICA is a low-yield diagnostic test. For example, analysis of the National Cardiovascular Data Registry CathPCI Registry done by Sahni and Tobis [2018] showed that only 40% of patients who underwent ICA had obstructive CAD. Moreover, the cost of ICA in comparison to simulation based methods that only require CTA is significantly higher [Darlington et al., 2015]. Hence, the unnecessary usage of ICA is needlessly expensive, which can be avoided by a simulation-based approach. For these reasons, ICA is only suitable for high-risk patients. Furthermore, the accuracy of ICA is limited: ICA tends to either underestimate or overestimate the severity of a stenosis [Borren et al., 2015, Skelly et al., 2016]. It should be noted that simulation based analysis methods still require data from CTA, which is not a completely non-invasive process, in that a dye must still be injected into the body through a vein in the arm; however, it is a far less invasive and expensive procedure in comparison to an ICA, which involves a catheter as aforementioned. Currently, simulation based diagnosis via CTA analysis has

comparable accuracy to that of ICA, and with improved understanding of the hemodynamics associated with CAD, simulation based diagnosis will become more accurate [Gorenoi et al., 2012].

The most popular non-invasive method for CAD diagnosis is the cardiac stress test [Kharabsheh et al., 2006]. The use of an electrocardiogram in tandem with a cardiac stress test is a common, non invasive method to diagnose CAD. However, occlusions, particularly in the LCX, are under diagnosed using this method [White et al., 2017]. Moreover, patients may be unable to perform exercise as part of the stress test. There are also several other factors that may result in poor electrocardiogram readings; for example, medications such as digoxin can result in false positive S-T segment fluctuations, while other abnormalities can result in uninterpretable results [Skelly et al., 2016]. Such false positives can have serious implications, and lead to unnecessary ICA which both introduces risk and is expensive.

LCX occlusions are responsible for 1 in every 5 myocardial infarctions (MI) [White et al., 2017]. Additionally, LCX occlusions have been found to present increased risk of heart failure and mortality in comparison to occlusions in the right coronary arteries and the left anterior descending arteries [Kozuch et al., 2015]. Given both the frequency and risks of CAD, it is clear that improving upon diagnosis methods is valuable. Therefore, due to the particularly high risk of LCX occlusions, an analysis of the hemodynamics associated with CAD in the LCX was conducted. Numerical simulations were conducted on a diseased LCX geometry and an artificially restored LCX geometry to represent the initially healthy vessel in order to identify hemodynamic patterns between the two geometries. The restoration technique used in this study was inspired by "Blood Flow Simulations of the Renal Arteries - Effect of Segmentation and Stenosis Removal", in which Berg et al. [2019] utilized Voronoi diagram based reconstruction and mesh sweep reconstruction to artificially remove stenosis in the renal arteries. In this study and others, a restoration procedure to artificially create a healthy vessel is used largely because it is both difficult and rare to have access to data of a patient before and after atherosclerotic stenosis. A potentially viable solution to this problem is to artificially repair the vessel geometry as done in this study. The findings of this analysis are relevant to CAD in the LCX as well as other blood vessels. Simulations were conducted using the open source cardiovascular simulation tool, SimVascular (SV), developed jointly by researchers at Stanford University and University of California, Berkeley [Updegrave et al., 2017].

The principle of artificially restoring a diseased vessel in order to conduct a hemodynamic study was also implemented by Li et al. [2018] in "Retrospective Study of Hemodynamic Changes Before and After Carotid Stenosis Formation by Vessel Surface Repairing", where an analysis of the hemodynamics associated with stenosis in the carotid artery was conducted. The carotid sinus was reconstructed and compared to the diseased vessel to gain further insight into the hemodynamics associated with atherosclerotic stenosis.

## 2 Data

The vessel geometry used for simulation is derived from the volumetric CTA data of a diseased LCX obtained from the Cardiovascular and Pulmonary Model Repository Corporation [2009]. A rendering of the CTA data is shown in figure 1.



Figure 1: Volumetric rendering of CTA Data

The CTA data encompasses a square-prism region with a base of 19.93 cm and a height of 12.6 cm; hence, the data covers a volume of  $5.00 \times 10^3 \text{ cm}^3$ .

The patient is a 65 year old male who is 64.3 inches tall and weighs 108.7 lbs. The patient's blood pressure is determined to be 131/68 mmHg, and the patient's cardiac output is determined to be 4.21 L/min [Ellwein-Fix et al., 2011]. The patient has CAD in the LCX, and underwent percutaneous coronary intervention (PCI). The obtained CTA data was taken preoperatively. The CTA data was processed and analyzed in SV, using a framework based on the Medical Imaging Interaction Toolkit. This framework allows the user to parse volumetric CTA data into the axial, sagittal, and coronal planes. This simplifies the process of defining the geometry of the LCX.

Data availability is a crucial factor in this area of research. If abundant datasets are made publicly available, it will enable large scale studies that can better validate hemodynamic patterns associated with CAD. The procedure in this study and others can be reiterated to identify the accuracy and tolerance of identified patterns in slightly different geometries. This will significantly improve the value of these studies as well as other approaches involving different techniques such as machine learning. Hence, limitations in data availability due to either privacy or commercialization greatly hinder progress in this field of

research.

### 3 Theory of Simulation

The primary goal of this research is to study the flow of blood in a diseased and restored LCX using the SV simulation tool. To model blood flow, SV solves the incompressible Navier-Stokes Equations,

$$\rho \frac{\partial \vec{v}}{\partial t} + \rho(\vec{v} \cdot \vec{\nabla})\vec{v} + \vec{\nabla}p - \vec{\nabla}\tau = 0 \quad (1)$$

$$\vec{\nabla} \cdot \vec{v} = 0 \quad (2)$$

where  $\rho$  is blood density,  $\vec{v}$  is the the velocity of the blood flow,  $p$  is the pressure, and  $\tau$  is the viscous portion of the stress tensor [Updegrove et al., 2017]. These are the standard Navier-Stokes equations solved in computational fluid dynamics. The numerical solver in SV uses a finite element discretization based on an unstructured mesh to obtain numerical solutions to the Navier-Stokes equations.

## 4 Simulation Setup

### 4.1 Defining a Path

[Lan et al., 2018] To create a model of the LCX, a path for the vessel must first be defined. In SV, a path is defined by two sets of points: control points, which are selected by the user, and path points that subdivide control points in regular intervals. Control points are chosen by tracing the vessel in the volumetric CTA data, which can be done by slicing the image along the axial planes as shown in figure 2. The approximate total number of path points is defined by the user. The two sets of points combined define a vessel path, where the path is defined by an interpolating spline, as shown in figure 3. To define the LCX path, 15 control points were defined, alongside a total of 106 path points.

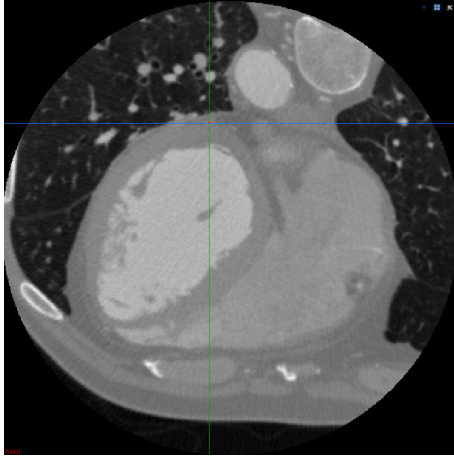


Figure 2: Tracing LCX on Axial Plane

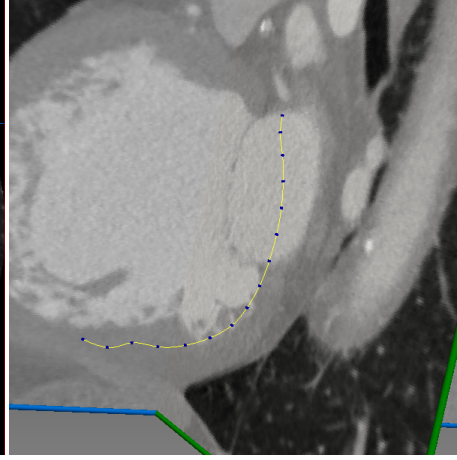


Figure 3: LCX Path

## 4.2 Segmentation and Modeling

To construct the vessel lumen, 2D segmentations representing the cross sections of the lumen are defined. SV renders an image of the plane perpendicular to the vessel path at a given point along the path. The path can be traversed using the image reslice probe. To segment the diseased LCX, 19 segments approximating the vessel cross-sections as circular were used as shown in figure 4. However, in order to accurately capture the diseased region, three segments in the diseased region were manually defined using a spline polygon as shown in figure 5. These segments were traced over the cross-sections of the model obtained from the Vascular Model Repository, which was constructed in further detail using optical coherence tomography (OCT) [Ellwein-Fix et al., 2011]. The set of segmentations are then lofted together with B-splines to create a solid model, as shown in figure 8.

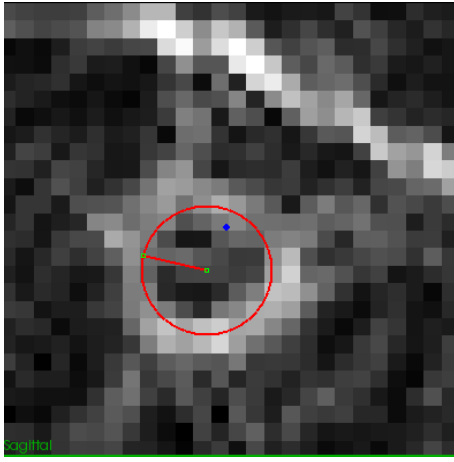


Figure 4: Circular Segmentation

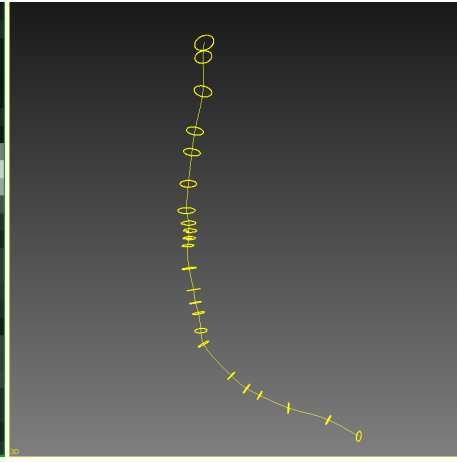


Figure 5: LCX Segmentation

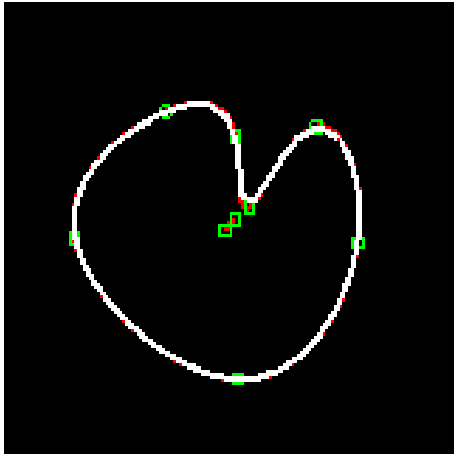


Figure 6: Segmentation using spline

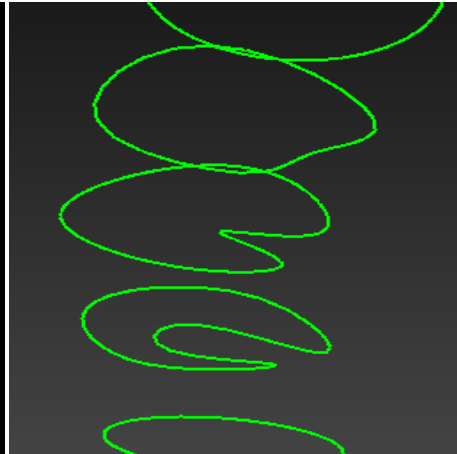


Figure 7: Diseased Segments

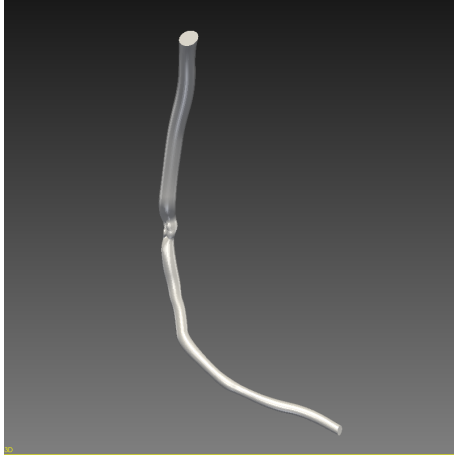


Figure 8: LCX Model

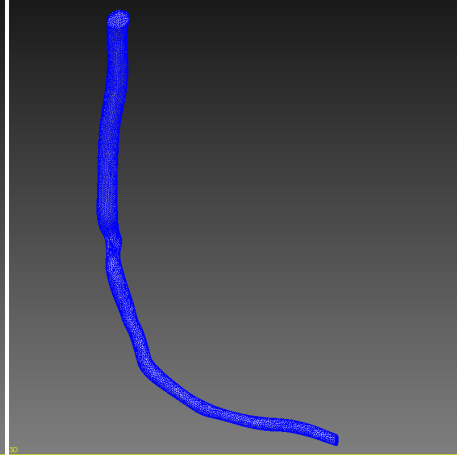


Figure 9: LCX Mesh

### 4.3 Meshing

The solid model is then used to create a 3-D mesh of the computational domain, resulting in discretization suitable for the numerical solver in SV. A tetrahedral mesh based on 3D Delaunay Triangulation [Si, 2015] is created for the LCX using SV. The mesh has 160272 tetrahedral elements, 30513 nodes, 30315 edges, and 20210 faces. The global maximum for the tetrahedron edge size is 0.0313 cm. The created mesh is shown in figure 9.

### 4.4 Conditions and Properties

A steady flow simulation was conducted (as opposed to pulsatile or Womersley flow), as it has been shown to be sufficient to describe the hemodynamics of coronary blood flow in stenosed vessels [Mates et al., 1978]. The dynamic viscosity of blood was defined as 0.04 poise, and the density of blood was defined as  $1.06 \frac{\text{g}}{\text{cm}^3}$ . A no-slip boundary condition was implemented, and the walls of the vessel were considered to be rigid.

#### 4.4.1 Inlet Boundary Conditions

A velocity is prescribed to the inlet to serve as a boundary condition. A parabolic inlet velocity profile was used. To determine the inlet flow rate, the patient's cardiac output was used. The cardiac output received by the LCX was calculated on the basis that the coronary arteries receive .05 of the total cardiac output, .84 of which is allocated to the left main coronary artery from which the LCX receives .33 [Ellwein-Fix et al., 2011]. The calculated values are shown in table 1.

Patient cardiac output	LCX fraction of output received	LCX output received
4.21 $\frac{\text{L}}{\text{min}}$	0.01386	0.97251 $\frac{\text{cc}}{\text{s}}$

Table 1: Inlet Boundary Condition Calculation

Hence, the inlet flow rate is 0.97251  $\frac{\text{cc}}{\text{s}}$ .

#### 4.4.2 Outlet Boundary Conditions

A resistance is assigned to the vessel, serving as an outlet boundary condition by making the face outlet into a weakly-pressure face. In this manner, the vessel obeys a form of Ohm’s Law for advective processes:

$$\Delta P = RQ$$

$\Delta P$  is the pressure drop across the vessel, which is analogous to voltage.  $R$  is the vessel resistance, which is analogous to the equivalent resistance of a circuit.  $Q$  is the volumetric flow rate, or received cardiac output, which is equivalent to current.

If the total peripheral resistance of blood flow in the patient is known, the ratio of the total cardiac output to the received cardiac output by the LCX can be used to determine the resistance of the LCX to be around 121953  $\frac{\text{dynes}\times\text{s}}{\text{cm}^5}$ .

#### 4.4.3 Time Step Calculation

To determine the time step size  $\Delta t$ , the Courant–Friedrichs–Lewy condition (CFL) is used to make the estimation. The CFL condition provides a relationship between the flow velocity, a temporal discretization parameter (time step size)  $\Delta t$ , and a mesh discretization parameter  $h$  [Updegrave et al., 2017]:

$$CFL = \frac{v\delta(t)}{h}$$

To obtain a reasonable time step size, the CFL number must be approximately 1.0 [Updegrave et al., 2017]. Using velocity calculated from the volumetric flow rate and the global maximum of the mesh element edge size for the mesh discretization parameter, the time step size is calculated to be 0.002 seconds.

Another factor must be considered: the number of time steps must provide sufficient time for the flow to reach a steady state. 500 time steps yields a physical time of 1 second, which is sufficiently long. The data is saved every 25 time steps.

## 5 Diseased Vessel Simulation Results

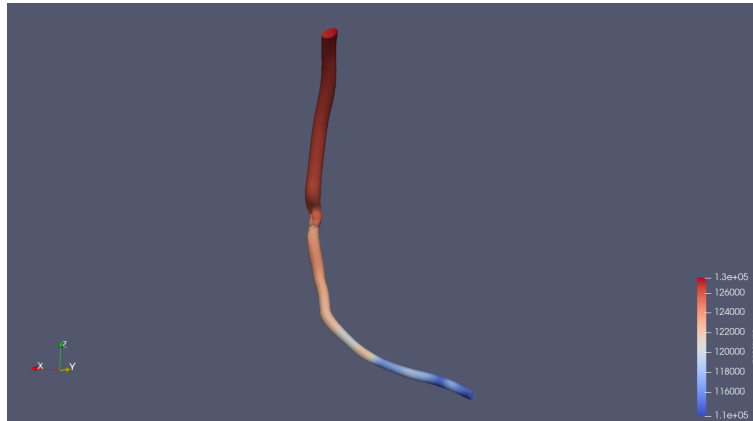


Figure 10: Pressure in LCX, Ba

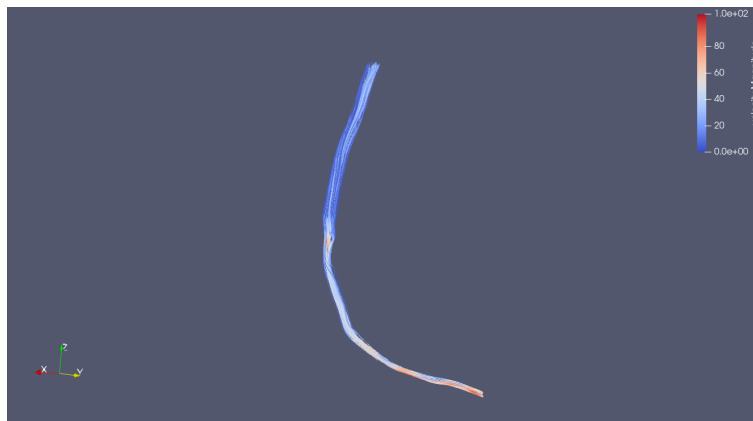


Figure 11: Velocity Streamlines in LCX,  $\frac{\text{cm}}{\text{s}}$

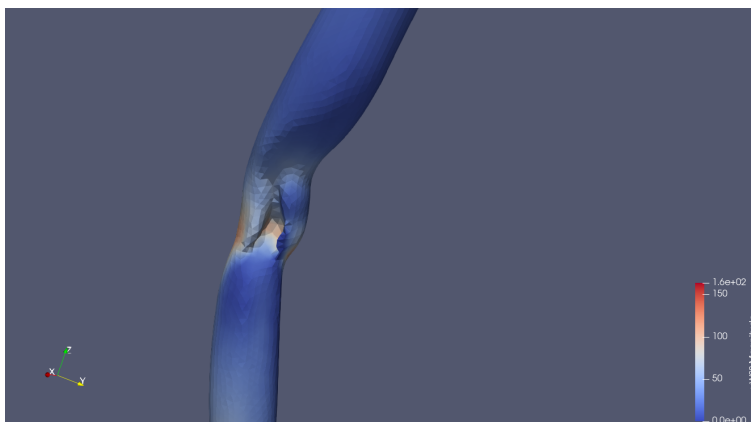


Figure 12: WSS in Diseased Region of LCX, Ba

Quantities such as pressure and velocity were extracted from the simulation files and were exported to the ParaView tool, which was used for post-processing and data visualization [Ahrens et al., 2005, Ayachit, 2015]. The resulting images from ParaView consist of calculated quantities, such as WSS, over the unstructured tetrahedral mesh. The graphs are volumetric, 3D plots of the calculated variables, and the corresponding color scale represents the values shown. In the pressure graph shown in figure 10, there is a pressure gradient ranging from  $1.1 \times 10^5$  Ba to  $1.3 \times 10^5$  Ba, which is a result of the assigned resistance boundary condition,  $R_{LCX}$ . A noticeable change in pressure occurs near the diseased region, where high pressure is clearly seen directly before and above the diseased region due to the reduced cross sectional area from the stenosis that developed. Lower pressure is hence observed below the diseased region. This is expected, as the velocity of blood through the diseased region is increased by the continuity equation due to decreased cross sectional area; therefore, a pressure reduction is reasonable considering Bernoulli's equation.

A similar pattern is observed in the velocity plot shown in figure 11 where flow velocity is lower before and above the diseased region due to the obstructive geometry of the stenosis. A local maximum in velocity is also observed in the diseased region due to the smaller cross sectional area of the vessel lumen as a result of the developed stenosis.

High WSS is observed in the diseased region, as shown in the shades of red featured in figure 12, reaching a maximum of 125.301 Ba. Again, this local maximum results from the obstructive geometry of the stenosis. Therefore, the expected results are achieved, in that the presence of CAD is disrupting the flow of blood through the LCX.

## 6 Vessel Restoration

The purpose of vessel restoration is to attempt to restore the diseased LCX to a geometry that accurately represents the healthy LCX before the development of CAD. This allows for an assessment of the hemodynamics in the formerly diseased region in order to determine potential dynamic factors that are associated with the development of CAD. In order to restore the diseased LCX, the three segments in the diseased region that were manually defined using a spline polygon to characterize the stenosis were removed, as shown in figure 14. These three segments were replaced by artificial, circular segments to represent a healthy vessel; this was done using a simplified version of mesh sweep reconstruction [Berg et al., 2019]. First, the centerline of the new vessel was computed and extracted as shown in figure 15. A linear function was used to determine the radius of circular segments that replace the diseased segments. These artificial segments are centered on the computed centerline, and have a radius determined by the function  $r = -.0035x + .288$  based on the mesh sweep reconstruction algorithm, where  $x$  is the reslice value when traversing through the vessel path using the image reslice probe. The artificial segments are shown in figure 16.

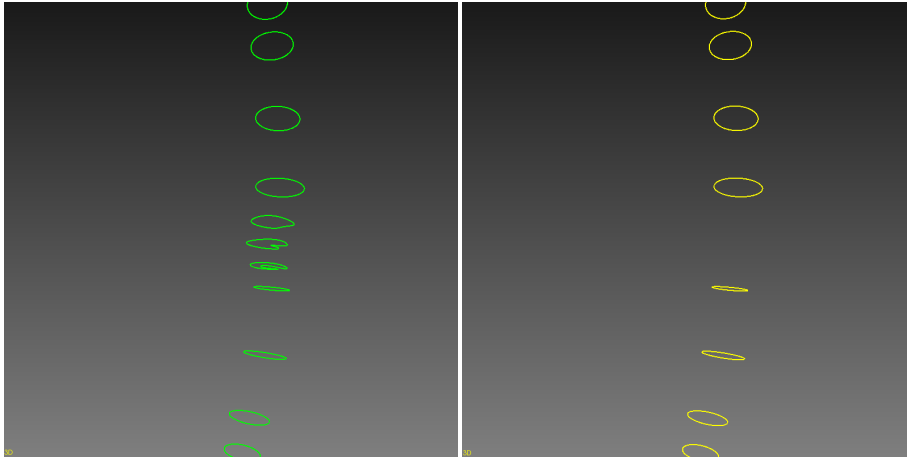


Figure 13: Diseased Segments

Figure 14: Diseased Segments Removed

The new segmentation is lofted to create the restored vessel's model. The restored model, figure 18 is shown in comparison to the diseased model 17.

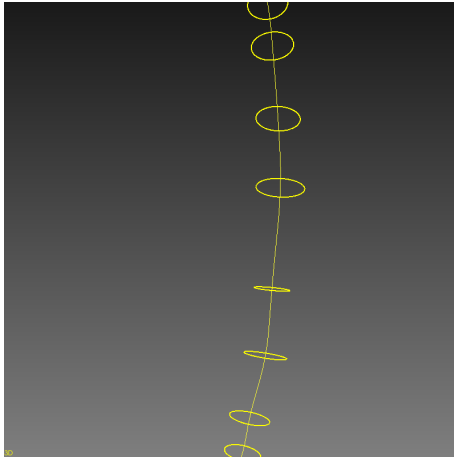


Figure 15: Centerline computed

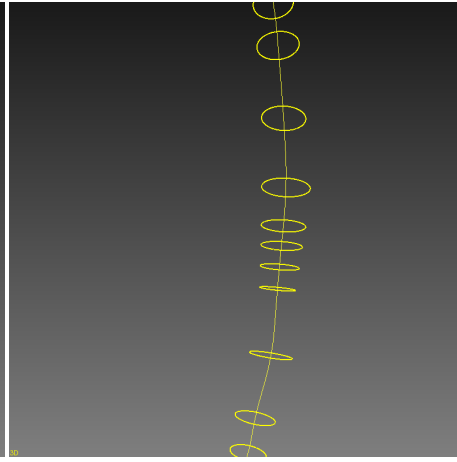


Figure 16: Artificial Segments Added

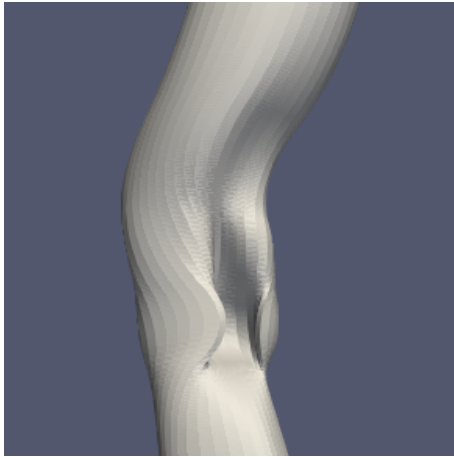


Figure 17: Pre-restoration model

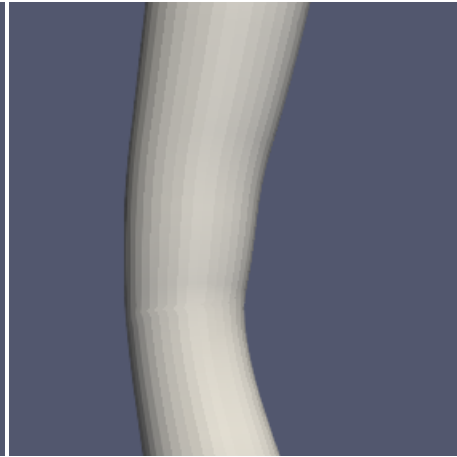


Figure 18: Post-restoration model

A new mesh is created for the restored model, and simulations are run on this mesh using the same boundary conditions and general properties as the previous simulation.

## 7 Results

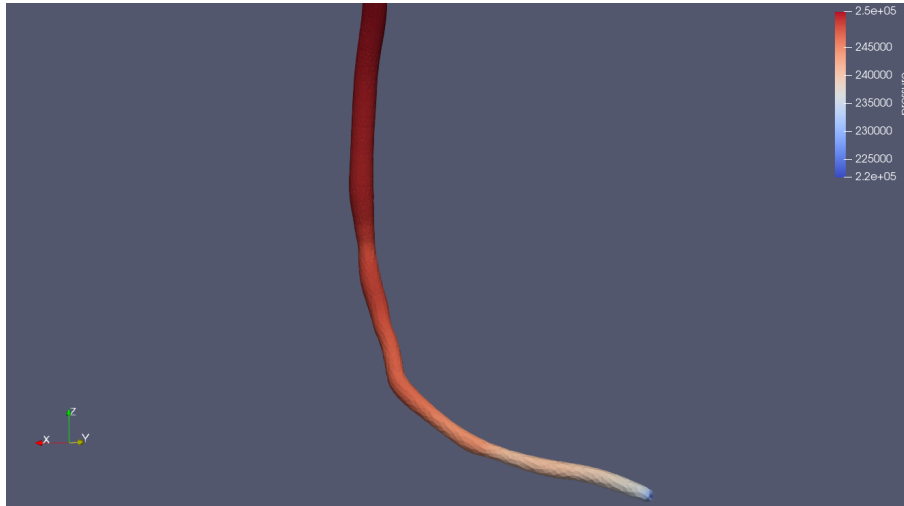


Figure 19: Pressure in Restored LCX, Ba

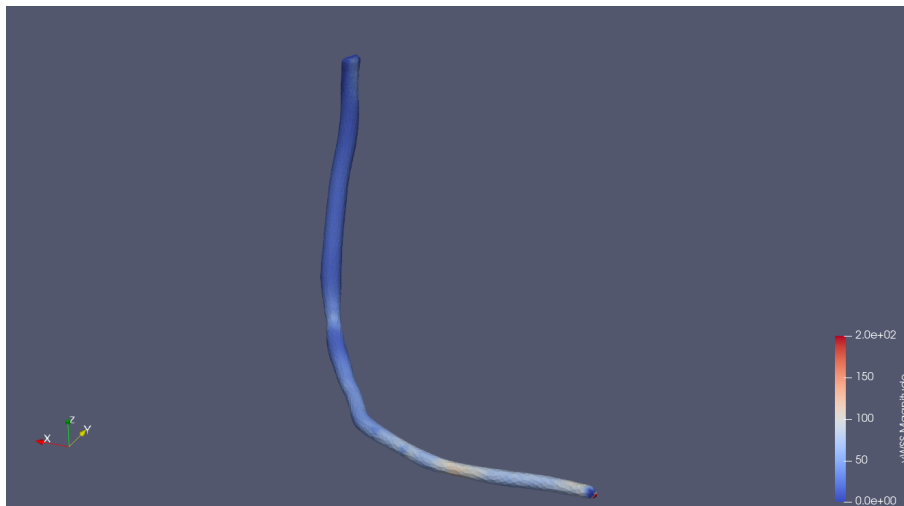


Figure 20: WSS in Restored LCX, Ba

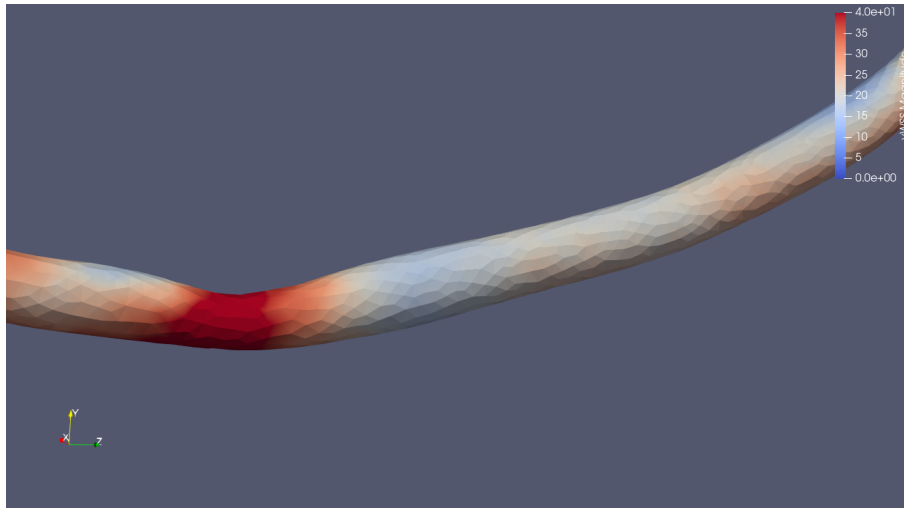


Figure 21: WSS in formerly diseased region of Restored LCX, Ba

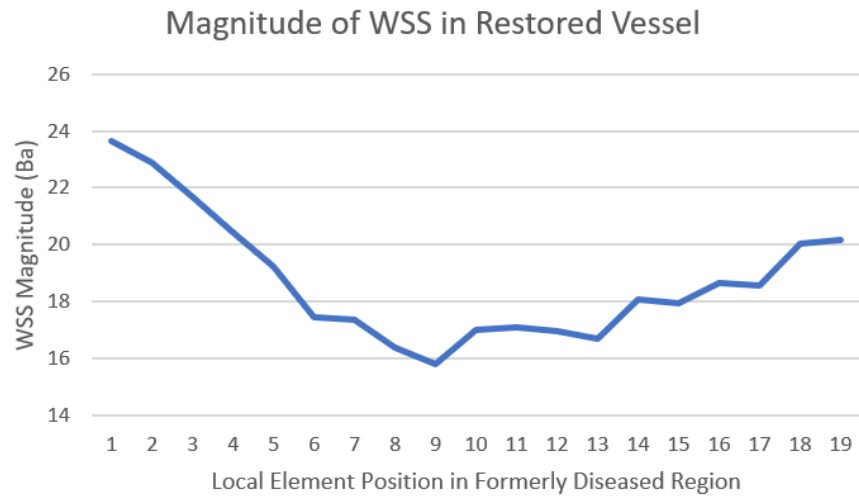


Figure 22: Plot of WSS in formerly diseased region of Restored LCX

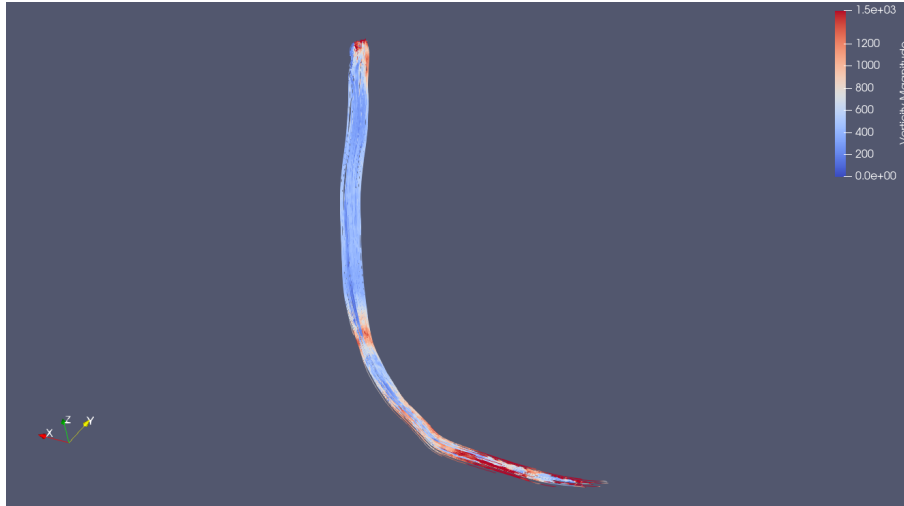


Figure 23: Vorticity in Restored LCX,  $s^{-1}$

In analyzing the simulation results of the restored vessel, comparisons are drawn between the hemodynamics of the restored vessel and the diseased vessel. In addition, abnormal characteristics of the flow in the formerly diseased region are observed.

Similar to the pressure graph of the diseased LCX shown in figure 10, a pressure gradient exists in the restored vessel shown in figure 19 ranging from  $2.2 \times 10^5$  Ba to  $2.5 \times 10^5$  Ba. More importantly, the pressure gradient present in the restored vessel is smooth as there are no obstructions present in the restored region, in contrast to the observed pressure drop at the diseased region in figure 10 representing the diseased LCX.

Upon restoration, the formerly diseased region features low WSS as shown in figures 20 and 21, in contrast with the high WSS in the diseased LCX shown in figure 12. Here, a local minimum in WSS of about 15.8 Ba is observed, as shown in figure 22; this is significantly smaller than the high WSS of 125.301 Ba observed in the diseased LCX. This is in agreement with the fact that CAD eventually developed in this region, given that low WSS is a well-established contributor to atherosclerosis and the development of CAD. Therefore, the low WSS characteristic of the restored geometry supports the general validity and accuracy of the restoration process, as this is an expected characteristic of a region that developed CAD.

An interesting characteristic is the presence of high vorticity in the region, as shown in figures 23 and 24. A single streamline passing through the formerly diseased region was selected, and a plot of vorticity along the entire streamline was generated (shown in figure 25). It is observed that the absolute maximum vorticity of  $1266.2 s^{-1}$  along the vessel lies at the formerly diseased region.

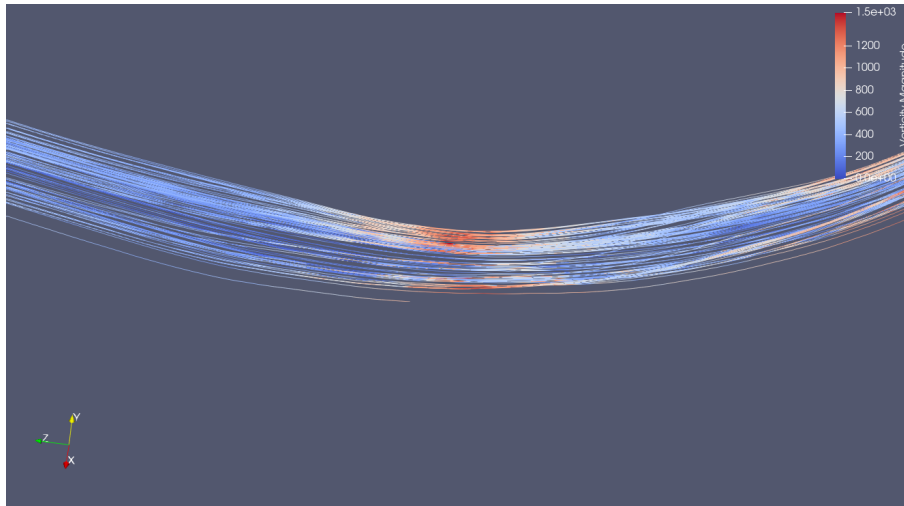


Figure 24: Vorticity in formerly diseased region of LCX,  $s^{-1}$

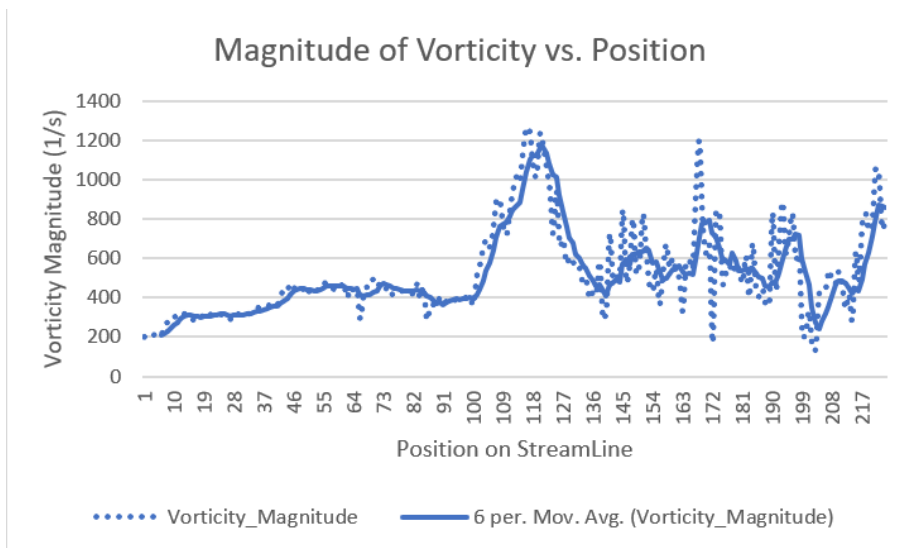


Figure 25: Magnitude of vorticity as a function of position

## 8 Further Investigation

The restoration technique used has its limitations in representing the initially healthy LCX of the patient. It is unlikely that the original, healthy geometry was smaller than the artificially restored geometry used in this study, simply

because a further contracted geometry would intrude into the boundaries of the stenosed vessel. However, it is possible that the true vessel was larger than the artificially restored vessel used in this study. To account for this possibility and examine the tolerance of the hemodynamic characteristics identified in the artificially restored model, the three initially diseased segments in the LCX model which were then artificially replaced with circular segments were further dilated. Each of the three segments were dilated by a certain  $\delta r$  relative to its radius,  $r$ . Relative tolerances of  $\frac{\delta r}{r} = 5\%$ ,  $10\%$ , and  $15\%$  were tested, as shown in table 2. The hemodynamic traits of the dilated geometries were compared to that of the original restored geometry in order to validate the characteristics that were already identified.

Dilation Factor	Initial Segment Radius (cm)			Final Segment Radius (cm)		
	Segment 1	Segment 2	Segment 3	Segment 1	Segment 2	Segment 3
5%	0.1270	0.1165	0.1095	0.1335	0.1223	0.1150
10%	0.1270	0.1165	0.1095	0.1397	0.1282	0.1205
15%	0.1270	0.1165	0.1095	0.1461	0.1340	0.1259

Table 2: Segment Dilation Calculations

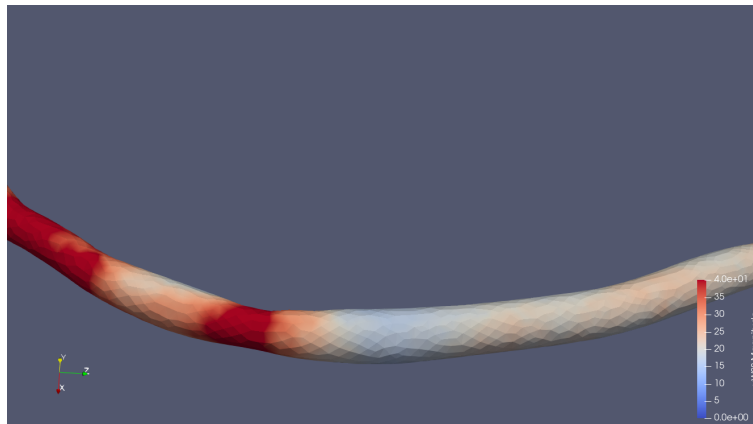


Figure 26: WSS in 5% dilated restoration geometry

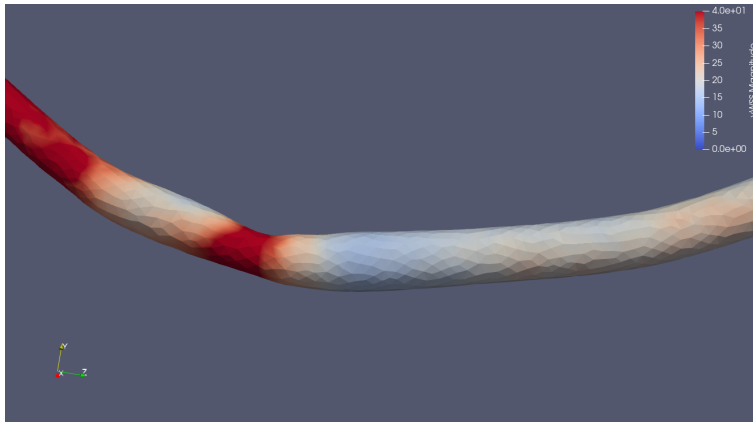


Figure 27: WSS in 10% dilated restoration geometry

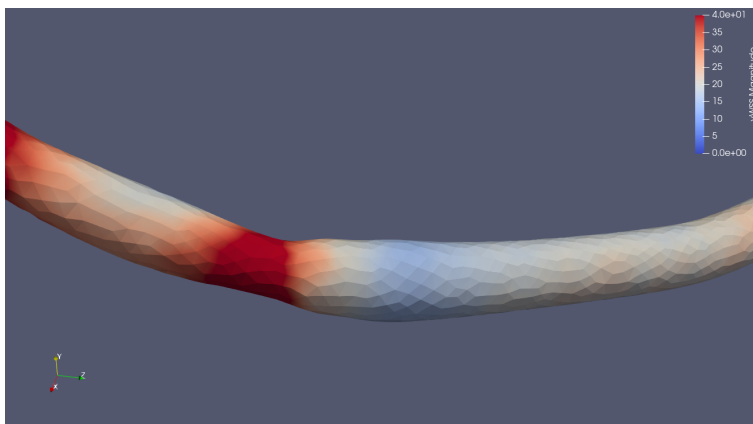


Figure 28: WSS in 15% dilated restoration geometry

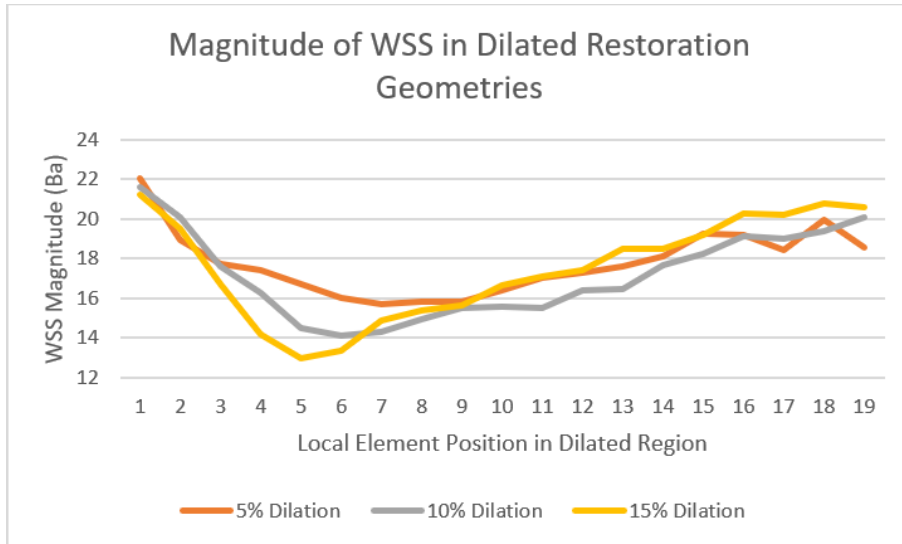


Figure 29: WSS in Dilated Restoration Geometries

There is a region of low WSS in the formerly diseased regions of the three dilated vessels, as indicated in the WSS plots shown in figures 26, 27, and 28. This is in agreement with the results from the standard restoration simulation, which also featured a local minimum in WSS. Furthermore, the geometries with larger dilation factors have lower minimum values of WSS in the dilated region, as illustrated in figure 29. The 15% dilated restoration geometry exhibits the lowest minimum WSS of 12.9665 Ba. The 10% dilated restoration geometry exhibits a minimum WSS of 14.1081 Ba. Meanwhile, the 5% dilated geometry exhibits the highest minimum WSS of 15.6945 Ba. Additionally, the minimum WSS in restoration geometries with larger dilation factors lies towards the distal end of the dilated region. The minimum WSS in the 15% dilated geometry is the most distal, whereas the minimum WSS in the 5% dilated geometry is the most proximal. This is indicated in the WSS plot in figure 29, the restored vessels with varying dilation factors are reaching the minimum WSS extrema at staggered intervals along the dilated region. It should also be noted that the observed minimum values of WSS in the dilated restoration geometries are all more extreme than the minimum WSS in the standard restoration geometry. This also suggests that dilated geometries are more susceptible to CAD, as they feature a more extreme region of low WSS.

The observed WSS trend can be logically supported. WSS is directly proportional to the gradient of the tangential component of velocity. Therefore, when increasing cross sectional area of the vessel lumen via dilation, velocity will decrease by the continuity equation, resulting in low WSS.

Similar to the standard restoration geometry, the dilated vessels also contained a region of high vorticity near the formerly diseased region, as shown in

figure 33. Repeating the procedure used for analyzing vorticity in the standard restoration geometry, a single streamline passing through the formerly diseased region was selected for each of the dilated vessels, and a plot of vorticity along the entire streamline was generated as shown in figure 25. It is observed that the maximum vorticity in the formerly diseased regions of the 5%, 10%, and 15% dilated geometries are  $1035.38 \text{ s}^{-1}$ ,  $1164.27 \text{ s}^{-1}$  and  $1386.51 \text{ s}^{-1}$  respectively. In this manner, the dilated vessels also exhibited an absolute maximum in vorticity in the same manner as the standard restored vessel, further validating vorticity as a characteristic associated with CAD in the LCX.

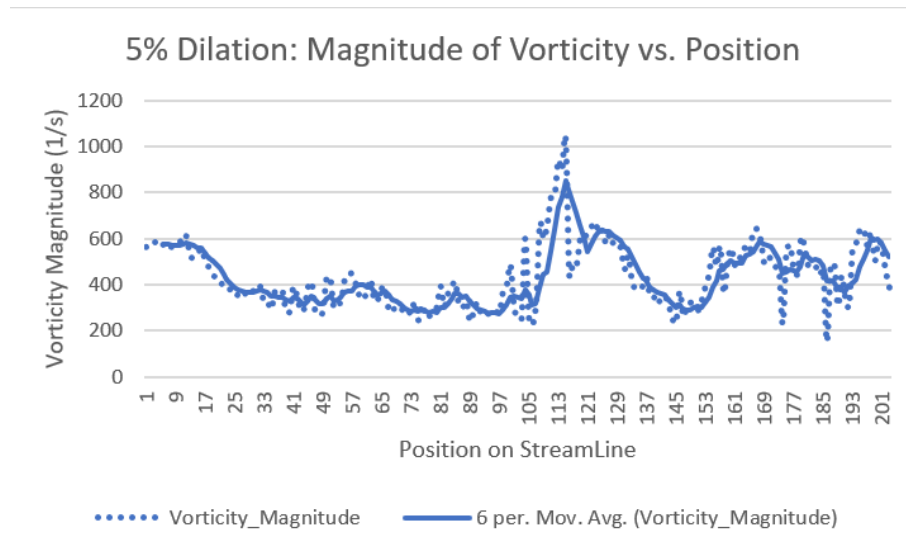


Figure 30: Magnitude of Vorticity in 5% dilated geometry

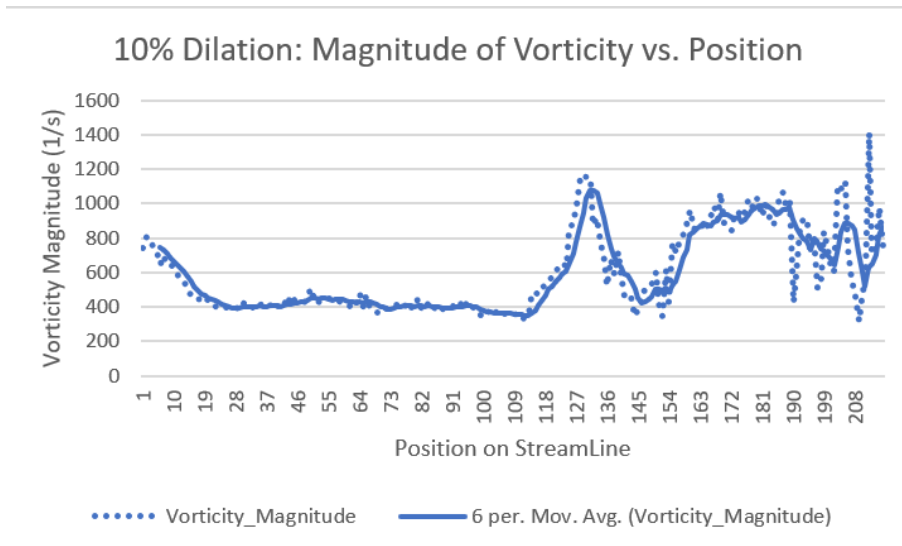


Figure 31: Magnitude of Vorticity in 10% dilated geometry

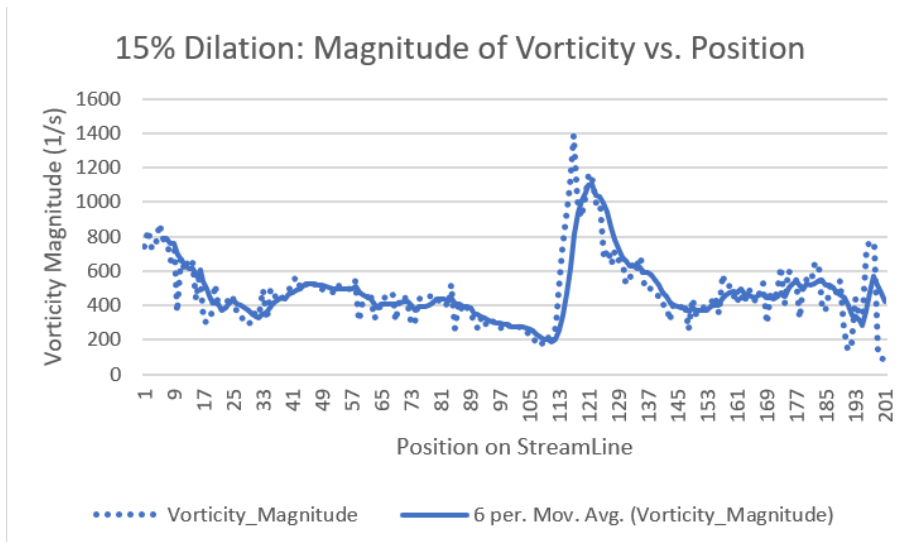


Figure 32: Magnitude of Vorticity in 15% dilated geometry

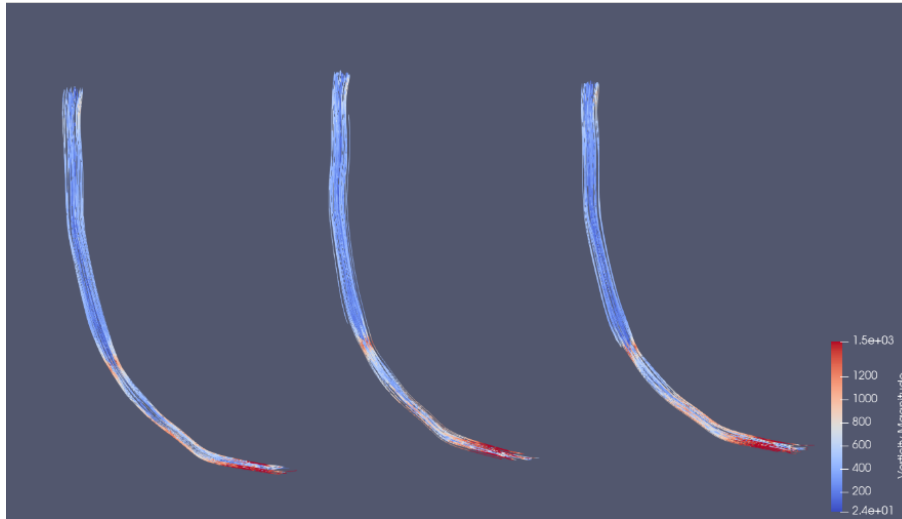


Figure 33: Vorticity in 5%, 10%, and 15% dilated geometries respectively,  $s^{-1}$

When analyzing the dilated restoration geometries, it is more clear that the region of high vorticity is found at the distal boundary of the dilated region, whereas in the standard restoration geometry, the region of high vorticity coincides more directly with the formerly diseased region. Hence, it is likely that the high vorticity characteristic contributes to the disturbed blood flow present in the dilated region, which in turn contributes to other atheroprone characteristics, such as low WSS, resulting in the development of CAD. Thus, the prominence of vorticity in these simulations suggests that vorticity is a relevant factor when evaluating the risk of CAD in a vessel.

## 9 Conclusion

Recent advancements in cardiovascular simulation software have enabled patient-specific simulation for individualized diagnosis and treatment planning. This is particularly valuable considering that the role of hemodynamics in any disease scenario is highly individualized [Updegrave et al., 2017]. Tools such as SV have been key in research on individualized medicine, surgical planning and medical device design [Updegrave et al., 2017]. Recently, CTA derived fractional flow reserve became the first and only simulation-based technology approved by the United States Food and Drug Administration for CAD diagnosis; this method is being implemented by HeartFlow Inc, in Redwood City, California [Nørgaard et al., 2019]. Other noninvasive methods based on machine learning and reduced order models have also been increasing in popularity [Douglas et al., 2015]. Such methods can be improved as further analysis of the hemodynamics associated with CAD is done.

In this study, an analysis of the hemodynamics in a diseased and restored

LCX was conducted. It was observed that the region in which CAD developed was initially a region featuring low WSS and high vorticity. The low WSS characteristic of the restored geometry provides general validation for the restoration process, as this is an expected characteristic of a region that developed CAD. This in turn suggests that artificially restoring diseased vessel geometries to its initially healthy state is a promising method for investigating hemodynamics associated with the development of CAD. The vorticity characteristic is of interest as it may be associated with the curvature of the vessel. It has been shown in other studies that lesser curvature regions are atheroprone, and feature disturbed blood flow [see Heo et al., 2014, Chiu and Chien, 2011, Nigro et al., 2011]. Risk for the development of CAD in these regions can be quantified using vorticity. Vorticity is defined as the curl of velocity:  $\nabla \times \vec{v}$ . In natural coordinates:

$$\zeta = -\frac{\partial V}{\partial n} + \frac{V}{R_n}$$

The first term is the vorticity resulting from shear, and the second term is the vorticity resulting from curvature of the path. As shown, vorticity is related to radius of curvature ( $R_n$ ). Hence, it is possible that vorticity may be used as a way to quantitatively analyze the risk of CAD development in lesser curvature. The procedure outlined in this study can be reused on more data to gain a generalized understanding and reinforce the relationship between vorticity and CAD in lesser curvature regions.

The initial simulation using the standard restoration geometry was validated by conducting simulations on dilated restoration geometries, where the artificially healthy segments was dilated by factors of 5%, 10%, and 15%. This was done to test the tolerance of the patterns identified earlier, given that the standard restoration geometry may not accurately capture the true healthy geometry of the patient. The geometries with larger dilation factors featured a more extreme minimum WSS in the formerly diseased region, suggesting they are more susceptible to the development of CAD. Similarly, the high vorticity characteristic identified in the standard restoration geometry was upheld in the dilated geometries. It is likely that the vorticity contributes to the disturbed blood flow in the formerly diseased region, which has been identified as an atheroprone trait in other studies.

Interestingly, the research done by Li et al. [2018] also reached very similar conclusions regarding the hemodynamics associated with atherosclerotic stenosis. In that study, low WSS, low velocity, and apparent vortex was observed in the formerly diseased region of the repaired carotid vessel geometry. These findings corroborate with the observed low WSS and high vorticity in this study, providing further validation for the identified flow characteristics that are associated with CAD. However, validation for the application of artificial reconstruction to study the hemodynamics of diseased vessels is still needed to confirm the accuracy of the observed patterns.

The findings of this study and others can be advanced and reinforced by analyzing more data; however, this can only be accomplished with increased

availability in public datasets. As aforementioned, the difficulties of obtaining the necessary data for analyzing the hemodynamics associated with CAD significantly limits this field of research. Steps have been taken in recent years to improve upon this: the National Institute of Health has recently released several large datasets, including the DeepLesion dataset created by Yan et al. [2018] which features over 32,000 CT images with a variety of lesions, accounting for 4,400 unique patients. This dataset was released with the intention of improving detection accuracy of lesions. While the DeepLesion dataset has improved the situation with public access to data in this field, it would be beneficial if a more focused dataset with CTA imaging of CAD patients were also made available. As further advancements in publicly-available datasets are made, CAD research, as well as the broader field of universal lesion detection can be advanced via machine learning methods [Yan et al., 2018].

To enable a more comprehensive analysis of the hemodynamics associated with CAD, the procedure used in this study can be modified, assuming the necessary data is available. First, it would be invaluable to analyze data from a large number of CAD patients for validation and more thorough pattern identification. It has also been shown that including side branches of the vessel in question improves the accuracy of WSS and pressure gradient calculations [Vardhan et al., 2019]. Hence, a potential improvement would be to include either the distal end of the LCX along with the second obtuse marginal artery or the entire coronary tree as part of the simulation process. Another potential improvement would be to implement pulsatile flow and a lumped parameter Windkessel model for the outlet boundary condition to more accurately represent blood flow through the coronary tree. Similarly, the elasticity of the vessel walls can be better represented by treating it as being deformable with uniform wall properties (Poisson's ratio, elastic modulus, etc).

The accuracy of the segmentations can also be improved by not resorting to circular approximations of the vessel lumen, which may in turn influence the hemodynamic characteristics of the blood flow. Accurate segmentations can be achieved only via higher quality imaging, such as an OCT. Furthermore, although the potentially inaccuracy of the restoration technique used in this study was largely accounted for by the dilation tests, it would be valuable to test the effects of minute changes to the geometry of both the diseased and restored vessel on the dynamics of the flow. In addition, if the vessel segmentations are not approximated as circles, the restoration technique used in this study (a linear radius function of position) will no longer be valid. Hence, Voronoi diagram based reconstruction or mesh sweep reconstruction will be necessary. The effects of these techniques on the hemodynamics that are observed can help validate the patterns identified in this study.

More research is necessary to better understand the relationships between vorticity, WSS, curvature, and the development of CAD. A potential avenue would be to study the fluid dynamics of flows in artificially generated vessels with varying curvature to search for vorticity and other more established characteristics of atheroprone regions, particularly in the lesser curvature of the vessel. Such simulations could help validate the findings in this study.

More fundamentally, rigorous biological explanations to these observed patterns are needed to confirm the relevance of the dynamics of blood flow and the development of CAD. Recent studies have involved protein kinase c zeta (PKC $\zeta$ ) activity and its role in atherosclerosis and eventually CAD [Nigro et al., 2011]. As the understanding of hemodynamic factors and their contributions to CAD become more clear, risk analysis, diagnosis and treatment for CAD will become more accurate and effective.

## References

- James Paul Ahrens, Berk Geveci, and Charles Chi Wang Law. Paraview: An end-user tool for large-data visualization. In *The Visualization Handbook*, 2005.
- Utkarsh Ayachit. *The ParaView Guide: A Parallel Visualization Application*. Kitware, Inc., Clifton Park, NY, USA, 2015. ISBN 1930934300.
- Emelia J. Benjamin, Paul Muntner, Alvaro Alonso, Marcio S. Bittencourt, Clifton W. Callaway, April P. Carson, Alanna M. Chamberlain, Alexander R. Chang, Susan Cheng, Sandeep R. Das, Francesca N. Delling, Luc Djousse, Mitchell S.V. Elkind, Jane F. Ferguson, Myriam Fornage, Lori Chaffin Jordan, Sadiya S. Khan, Brett M. Kissela, Kristen L. Knutson, Tak W. Kwan, Daniel T. Lackland, Tené T. Lewis, Judith H. Lichtman, Chris T. Longenecker, Matthew Shane Loop, Pamela L. Lutsey, Seth S. Martin, Kunihiro Matsushita, Andrew E. Moran, Michael E. Mussolino, Martin O’Flaherty, Ambarish Pandey, Amanda M. Perak, Wayne D. Rosamond, Gregory A. Roth, Uchechukwu K.A. Sampson, Gary M. Satou, Emily B. Schroeder, Svati H. Shah, Nicole L. Spartano, Andrew Stokes, David L. Tirschwell, Connie W. Tsao, Mintu P. Turakhia, Lisa B. VanWagner, John T. Wilkins, Sally S. Wong, and Salim S. Virani. Heart disease and stroke statistics&#x2014;2019 update: A report from the american heart association. *Circulation*, 139(10):e56–e528, 2019. doi: 10.1161/CIR.0000000000000659. URL <https://www.ahajournals.org/doi/abs/10.1161/CIR.0000000000000659>.
- Niclas Berg, Laszlo Fuchs, and Lisa PrahL Wittberg. Blood Flow Simulations of the Renal Arteries - Effect of Segmentation and Stenosis Removal. *Flow, Turbulence and Combustion*, 102:27–41, 01 2019.
- Nanette M Borren, Angela H.E.M. Maas, and Jan Paul Ottervanger. Stop invasive coronary angiography as the gold standard for the diagnosis of stable angina. 2015.
- J. J. Chiu and S. Chien. Effects of disturbed flow on vascular endothelium: pathophysiological basis and clinical perspectives. *Physiol. Rev.*, 91(1):327–387, Jan 2011.

Open Source Medical Software Corporation. Cardiovascular and Pulmonary Model Repository, 2009. URL <http://www.vascularmodel.com/sandbox/doku.php?id=company>.

M. Darlington, P. Gueret, J. P. Laissy, A. F. Pierucci, H. Maoulida, C. Quelen, R. Niarra, G. Chatellier, and I. Durand-Zaleski. Cost-effectiveness of computed tomography coronary angiography versus conventional invasive coronary angiography. *Eur J Health Econ*, 16(6):647–655, Jul 2015.

S. S. Dhawan, R. P. Avati Nanjundappa, J. R. Branch, W. R. Taylor, A. A. Quyyumi, H. Jo, M. C. McDaniel, J. Suo, D. Giddens, and H. Samady. Shear stress and plaque development. *Expert Rev Cardiovasc Ther*, 8(4):545–556, Apr 2010.

P. S. Douglas, G. Pontone, M. A. Hlatky, M. R. Patel, B. L. Norgaard, R. A. Byrne, N. Curzen, I. Purcell, M. Gutberlet, G. Rioufol, U. Hink, H. W. Schuchlenz, G. Feuchtner, M. Gilard, D. Andreini, J. M. Jensen, M. Hadamitzky, K. Chiswell, D. Cyr, A. Wilk, F. Wang, C. Rogers, B. De Bruyne, A. Bartorelli, D. Andreini, M. Pepi, E. Bertella, S. Mushtaq, V. Beltrama, A. Baggiano, S. Gaur, L. Romby, J. R. Broderick, L. Hjelm, R. Byrne, E. Guerra, O. Husser, T. Koppa, J. Nadjiri, M. Hadamitzky, J. Winogradow, J. Repp, S. Weigand, F. Wimbaur, R. Lohaus, P. M. Rumpf, E. Lorenz, G. Schoemig, K. Hosl, J. Ruf, N. Curzen, J. Shambrook, S. Corbett, I. Simpson, A. Calver, J. Wilkinson, Z. Nicholas, J. A. Radmore, B. Tyrell, C. Elridge, R. Lacoste, I. Purcell, R. Das, I. Haq, A. G. Zaman, I. Spyridopoulos, A. Bagnall, J. Ahmed, A. Narytnyk, J. Adams-Hall, L. Bremner, S. Hetherington, S. Lamb, A. Phillipson, R. Wilson, K. Procter, S. Jones, V. A. Richardson, L. Quinn, V. Wealleans, S. Rowling, C. Price, M. Gutberlet, L. Lehmkuhl, M. Woinke, G. Schuler, D. Urban, C. L?cke, F. Juhlich, K. Luderer, J. Fohlisch, C. Dohnert, G. Rioufol, G. Finet, P. Douek, Y. Varillon, D. Laval, A. Mansuy, P. Renaudin, M. Rageade, U. Hink, K. Kreitner, A. Jabs, Y. Yang, T. Gori, B. Kaesberger, H. Schuchlenz, D. Botegal, M. Genger, P. Zechner, W. Weihs, P. Kullnig, W. Kau, S. Weikl, G. Feuchtner, G. Friedrich, F. Plank, M. Gilard, J. Boschat, P. Castellant, R. Didier, F. Martin, P. S. Douglas, B. De Bruyne, M. Hlatky, B. L. Norgaard, M. Patel, G. Pontone, C. Rogers, M. Patel, M. Patel, W. S. Jones, R. Shah, G. Dunn, A. Lowe, B. Martinez, A. Debus, J. Jaeger, F. Wang, and A. Wilk. Clinical outcomes of fractional flow reserve by computed tomographic angiography-guided diagnostic strategies vs. usual care in patients with suspected coronary artery disease: the prospective longitudinal trial of FFR(CT): outcome and resource impacts study. *Eur. Heart J.*, 36(47):3359–3367, Dec 2015.

Laura Ellwein-Fix, Hiromasa Otake, Timothy Gundert, Bon-Kwon Koo, Toshiro Shinke, Yasuhiro Honda, Junya Shite, and John LaDisa. Optical coherence tomography for patient-specific 3d artery reconstruction and evaluation of wall shear stress in a left circumflex coronary artery. *Cardiovascular Engineering and Technology*, 2:212–227, 09 2011. doi: 10.1007/s13239-011-0047-5.

- V. Gorennoi, M. P. Schnermark, and A. Hagen. CT coronary angiography vs. invasive coronary angiography in CHD. *GMS Health Technol Assess*, 8:Doc02, 2012.
- K. S. Heo, K. Fujiwara, and J. Abe. Shear stress and atherosclerosis. *Mol. Cells*, 37(6):435–440, Jun 2014.
- Eddie Hulten and Daniel William Carlson. *Invasive Coronary Angiography*, pages 77–89. Springer London, London, 2013.
- S. M. Kharabsheh, A. Al-Sugair, J. Al-Buraiki, and J. Al-Farhan. Overview of exercise stress testing. *Ann Saudi Med*, 26(1):1–6, 2006.
- M. Kozuch, P. Kralisz, M. Rog-Makal, H. Bachorzewska-Gajewska, and S. Dobrzycki. Significant narrowing of the circumflex artery leads to worse outcomes than right coronary artery narrowing in patients with anterior myocardial infarction treated invasively. *Neth Heart J*, 23(5):258–262, May 2015.
- H. Lan, A. Updegrove, N. M. Wilson, G. D. Maher, S. C. Shadden, and A. L. Marsden. A Re-Engineered Software Interface and Workflow for the Open-Source SimVascular Cardiovascular Modeling Package. *J Biomech Eng*, 140(2), 02 2018.
- Xiao Li, Beibei Sun, Huilin Zhao, Xiaoqian Ge, Fuyou Liang, Xuanyu Li, Jianrong Xu, and Xiaosheng Liu. Retrospective study of hemodynamic changes before and after carotid stenosis formation by vessel surface repairing. *Scientific Reports*, 8(5493), 04 2018. doi: 10.1038/s41598-018-23842-0. URL <https://doi.org/10.1038/s41598-018-23842-0>.
- R E Mates, R L Gupta, A C Bell, and F J Klocke. Fluid dynamics of coronary artery stenosis. *Circulation Research*, 42(1):152–162, 1978. doi: 10.1161/01.RES.42.1.152. URL <https://www.ahajournals.org/doi/abs/10.1161/01.RES.42.1.152>.
- P. Nigro, J. Abe, and B. C. Berk. Flow shear stress and atherosclerosis: a matter of site specificity. *Antioxid. Redox Signal.*, 15(5):1405–1414, Sep 2011.
- Bjarne L. Nørgaard, Timothy A. Fairbairn, Robert D. Safian, Mark G. Rabbat, Brian Ko, Jesper M. Jensen, Koen Nieman, Kavitha M. Chinnaiyan, Niels Peter Sand, Hitoshi Matsuo, Jonathon Leipsic, and Gilbert Raff. Coronary ct angiography-derived fractional flow reserve testing in patients with stable coronary artery disease: Recommendations on interpretation and reporting. *Radiology: Cardiothoracic Imaging*, 1(5):e190050, 2019. doi: 10.1148/ryct.2019190050. URL <https://doi.org/10.1148/ryct.2019190050>.
- K. H. Parker. A brief history of arterial wave mechanics. *Med Biol Eng Comput*, 47(2):111–118, Feb 2009.

- Sheila Sahni and Jonathan M. Tobis. Decision-Making for Invasive Coronary Angiography in Patients With SIHD: An Interventionalist’s Perspective. *American College of Cardiology*, Jan 2018.
- Hang Si. Tetgen, a delaunay-based quality tetrahedral mesh generator. *ACM Trans. Math. Softw.*, 41(2), February 2015. ISSN 0098-3500. doi: 10.1145/2629697. URL <https://doi.org/10.1145/2629697>.
- Andrea C Skelly, Robin Hashimoto, David I Buckley, Erika D Brodt, North Noelck, Annette M Totten, Jonathan R Lindner, Rongwei Fu, and PharmD Marian McDonagh. *Noninvasive Testing for Coronary Artery Disease*. Agency for Healthcare Research and Quality, Rockville, MD, US, Mar 2016.
- Antonio V. Sterpetti. Cardiovascular research by leonardo da vinci (1452&#x2013;1519). *Circulation Research*, 124(2):189–191, 2019. doi: 10.1161/CIRCRESAHA.118.314253. URL <https://www.ahajournals.org/doi/abs/10.1161/CIRCRESAHA.118.314253>.
- A. Updegrove, N. M. Wilson, J. Merkow, H. Lan, A. L. Marsden, and S. C. Shadden. SimVascular: An Open Source Pipeline for Cardiovascular Simulation. *Ann Biomed Eng*, 45(3):525–541, 03 2017.
- Madhurima Vardhan, John Gounley, S. James Chen, Andrew M. Kahn, Jane A. Leopold, and Amanda Randles. The importance of side branches in modeling 3D hemodynamics from angiograms for patients with coronary artery disease. *Scientific Reports*, 9(8854), 06 2019.
- Noah White, Gregory Wu, and Christopher Hanowitz. Left Circumflex Artery Occlusions: (Electrically) Silent but Deadly. *Emergency Medicine Residents’ Association*, 2017. URL <https://www.emra.org/emresident/article/left-circumflex-artery-occlusions-electrically-silent-but-deadly/>.
- Ke Yan, Xiaosong Wang, Le Lu, and Ronald M. Summers. DeepLesion: automated mining of large-scale lesion annotations and universal lesion detection with deep learning. *Journal of Medical Imaging*, 5(3):1 – 11, 2018. doi: 10.1117/1.JMI.5.3.036501. URL <https://doi.org/10.1117/1.JMI.5.3.036501>.